Universität Karlsruhe (TH)
Institut für Baustatik

Simulation of Delamination in Stringer Stiffened Fiber-Reinforced Composite Shells

W. Wagner, C. Balzani

Mitteilung 2(2006)

Universität Karlsruhe (TH)
Institut für Baustatik

Simulation of Delamination in Stringer Stiffened Fiber-Reinforced Composite Shells

W. Wagner, C. Balzani

Mitteilung 2(2006)

Prof. Dr.–Ing. W. Wagner
Institut für Baustatik
Universität Karlsruhe
Postfach 6980
76128 Karlsruhe

Telefon: (0721) 608–2280
Telefax: (0721) 608–6015
E–mail: bs@.uni-karlsruhe.de
Internet: http://www.bs.uni-karlsruhe.de

Simulation of Delamination in Stringer Stiffened Fiber-Reinforced Composite Shells

W. Wagner, C. Balzani
Institut für Baustatik
Universität Karlsruhe (TH)
Kaiserstraße 12
76131 Karlsruhe
Germany

Contents

Abstract

Fiber-reinforced composites are often used for high performance lightweight structures. For an enhanced exploitation of material reserves, fracture mechanisms should be taken into consideration. In this work, delamination and skin-stringer separation are examined in the framework of the finite element method. A cohesive interface element is used which is written in stress-strain relationships. The cohesive law rests upon a Smith-Ferrante type free energy function. It is edited so that only tensile normal or shear stresses provoke damage and contact is accounted for by an additional penalty term. Some numerical examples show the applicability of the proposed model.

1 Introduction

Fiber-reinforced plastics (FRPs) are often used for high performance structures since this material combines high stiffness, high strength and low weight. The application area ranges from sports utilities to airframe structures such as tennis rackets, bicycles, wings or airfoil parts, rotor blades etc. First attempts have also been made to use FRPs for aircraft fuselage structures. Composite laminates are highly customizable because fiber orientations can be adapted to any particular stress state. For optimal exploitation of material reserves, several fracture scenarios should be taken into consideration during the design phase.

Failure in laminated composites can be caused by intralaminar fracture (e.g. fiber fracture, transverse matrix cracking, fiber-matrix debonding, fiber buckling, etc.) or interlaminar fracture, namely delamination. Delamination is one of the most frequent failure modes in FRPs due to their lack of reinforcement in thickness direction. On the other hand interlaminar failure is especially dangerous because it can lead to a significant reduction of the load-carrying capacity in absence of any visible damage. Hence, delaminations should be accounted for in the design phase which requires reliable and robust simulation tools.

There are two main targets in the numerical treatment of delamination: Simulation of i) delamination initiation and ii) delamination propagation. Delamination onset is usually predicted using stress-strength based criteria [1]. Since geometrical discontinuities often lead to highly over-estimated stresses, predictions incorporating solely such criteria are not reliable. Thus, fracture mechanics approaches are often employed. The most prominent fracture mechanics approach is the virtual crack closure technique (VCCT) which has been proposed by Rybicki & Kanninen [2]. Here, energy-based criteria are used to predict delamination propagation. The VCCT has also been applied to the simulation of skin-stiffener debonding [3]. The method is computational effective. However, fracture mechanics approaches need pre-defined cracks which might be difficult to specify for complex geometries.

Another efficient method is the meso-level cohesive zone approach. It goes back to Dugdale [4] and Barenblatt [5]. Here, an extended crack tip is generated by introducing interfacial softening into a cohesive constitutive law. This reduces the difficulties related to high stress gradients at the crack front. An incorporation of the cohesive zone approach is straightforward if used in conjunction with so-called cohesive interface elements. Usually, interface elements relate interfacial tractions to relative displacements [6, 7, 8]. Borg et al. [9] formulated interface elements similar to nonlinear springs located in the element nodes. Surface-like zero-thickness interface elements have been proposed by e.g. de Borst & Schipperen [10], Shet & Chandra [11] and Zou et al. [12, 13] among many others. Interface elements with initial thickness have also been developed by Wagner et al. [14]. Cohesive laws are very close to continuum damage mechanics. If the area under the cohesive law is equal to the fracture toughness, the model combines stress-based criteria for the prediction of delamination onset and energy-based criteria for the prediction of delamination growth which are also used in fracture mechanics approaches. Needleman [15] considered cohesive elements especially attractive when the interfacial strength is relatively weak compared to the adjoining material, as is the case for FRPs. A certain restriction is that these elements have to be added to the discretization in advance. Thus, interface elements are peculiarly suitable when crack path or crack regions are expectable. In addition, the topological site and the shape of the crack tip are an outcome of the analysis.

In this paper, delamination and skin-stringer separation are treated in the same manner. A finite element formulation is developed which is able to predict both delamination and skin-stringer separation for various mixed mode loading conditions. In section 2, the governing equations of the finite element formulation are established. An irreversible cohesive law is derived in section 4, based on publications of DE-ANDRÉS ET AL. [16] and ORTIZ & PANDOLFI [17]. We make use of a continuous cohesive free energy function of Smith-Ferrante type [18]. This free energy function is edited in a way that only tensile normal stresses and shear stresses provoke delamination. Furthermore, a penalty term is added which avoids the interpenetration of the crack faces. The softening behavior is governed by exponential degradation. It is history dependent so stiffness degradation is irreversible. The model detects where delamination initiates and is able to predict propagating delaminations. Some numerical examples are carried out in section 5 which demonstrate the applicability of the proposed concept.

2 Finite Element Formulation

In this section, a cohesive interface element is derived which is able to predict the fracture process of delamination. For the following considerations, we assume that the hypothesis of MOHR [19] that fracture is caused by the stresses acting on the fracture plane is valid for the case of delamination. From this it follows that only interlaminar stresses trigger delaminations. These are namely the two shear stresses and the normal stress acting on the interface between two adjacent layers of laminated composites. This assumption has also been stated by HASHIN [20].

Usually, cohesive interface elements are formulated in terms of tractions and relative displacements between two surfaces, e.g. [21, 22] among many others. These surfaces are initially coincident with the real interface between two laminate layers. In this work, we follow the alternative approach proposed in [14]. The element derived here is based on the formulation of a standard hexahedral isoparametric solid element but carries only the interlaminar stresses. All other stresses are set to zero a priori. The initial thickness h_0 may be sufficiently thin so that the mechanical behavior is surface-like and the global response of the bulk material is not influenced as long as the interface is intact.

Fig. 1 shows an 8-noded interface element in the reference and the current configuration. The interlaminar stresses and strains are measured in a local rectangular coordinate system which is located at the element's midpoint. The local basis vectors $\boldsymbol{s}$, $\boldsymbol{t}$ and $\boldsymbol{n}$ are calculated from diagonal vectors, see TAYLOR [23]

$$\boldsymbol{d}_1 = \frac{\boldsymbol{c}_3 - \boldsymbol{c}_1}{|\boldsymbol{c}_3 - \boldsymbol{c}_1|} \,, \qquad \boldsymbol{d}_2 = \frac{\boldsymbol{c}_2 - \boldsymbol{c}_4}{|\boldsymbol{c}_2 - \boldsymbol{c}_4|} \,, \qquad \boldsymbol{c}_i = \frac{1}{2}(\boldsymbol{P}_i + \boldsymbol{P}_{i+4}) \,, \quad i = 1, ..., 4 \,. \tag{1}$$

Here, $\boldsymbol{s}$ and $\boldsymbol{t}$ are the local in-plane vectors and $\boldsymbol{n}$ is the local normal vector of the interlaminar interface, see Fig. 1.

$$\boldsymbol{s} = \frac{\boldsymbol{d}_1 + \boldsymbol{d}_2}{|\boldsymbol{d}_1 + \boldsymbol{d}_2|} \,, \qquad \boldsymbol{t} = \frac{\boldsymbol{d}_1 - \boldsymbol{d}_2}{|\boldsymbol{d}_1 - \boldsymbol{d}_2|} \,, \qquad \boldsymbol{n} = \boldsymbol{s} \times \boldsymbol{t} \,. \tag{2}$$

The global position vectors $\boldsymbol{P}$ and $\boldsymbol{P}_0$ are measured in a rectangular coordinate system spanned by the Euclidean basis vectors $\boldsymbol{e}_i$. Thus a local position vector in the reference

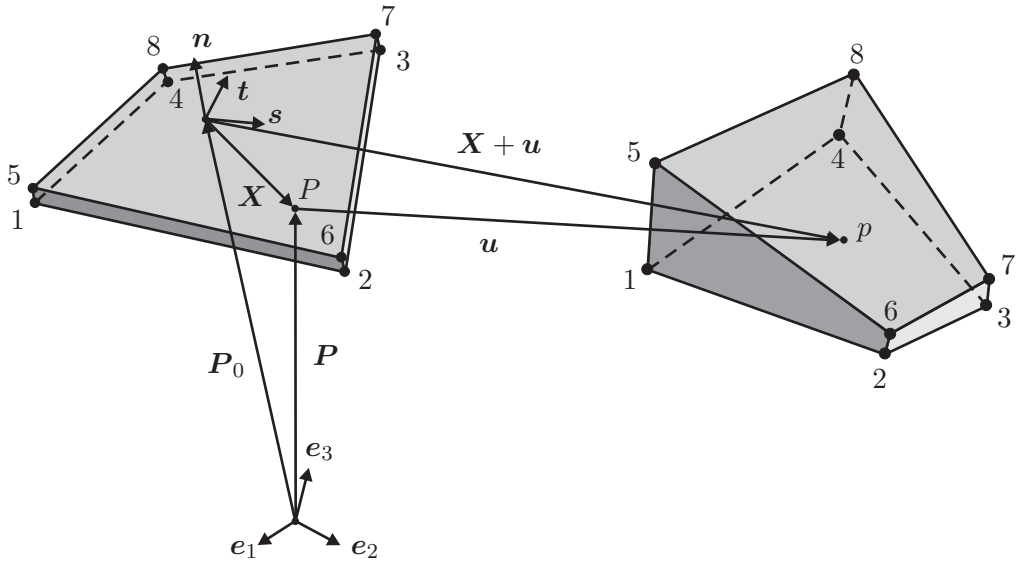

Figure 1: Reference and current configuration of the interface element.

configuration and in the current configuration are defined by

$$\boldsymbol{X} = \begin{bmatrix} X_s \\ X_t \\ X_n \end{bmatrix} = \boldsymbol{T}(\boldsymbol{P} - \boldsymbol{P}_0)\,, \quad \text{with} \quad \boldsymbol{T} = \begin{bmatrix} \boldsymbol{s} \\ \boldsymbol{t} \\ \boldsymbol{n} \end{bmatrix} \tag{3}$$

$$\boldsymbol{x} = \boldsymbol{X} + \boldsymbol{u}\,. \tag{4}$$

with the associated displacement vector

$$\boldsymbol{u} = [u_s, u_t, u_n]^T\,. \tag{5}$$

Taken into account only the interlaminar components, the three-dimensional stress and strain tensors reduce to interlaminar stress and strain vectors defined by

$$\boldsymbol{\sigma} = \begin{bmatrix} \tau_{sn} \\ \tau_{tn} \\ \sigma_n \end{bmatrix}\,, \qquad \boldsymbol{\varepsilon} = \begin{bmatrix} \gamma_{sn} \\ \gamma_{tn} \\ \varepsilon_n \end{bmatrix} = \begin{bmatrix} u_{s,n} + u_{n,s} \\ u_{t,n} + u_{n,t} \\ u_{n,n} \end{bmatrix}\,. \tag{6}$$

Obviously, a geometrically linear formulation has been chosen, which is no restriction. Since the interface element is surrounded by the bulk material, loading-type boundary conditions can be excluded. For isothermal quasi-static conditions the interface contribution to the principle of virtual work writes

$$\delta\Pi_{if}(\boldsymbol{u}) = \int_V \delta\boldsymbol{\varepsilon}^T\boldsymbol{\sigma}\;\mathrm{d}V\,, \tag{7}$$

where V is the volume of the interface and $\delta\boldsymbol{\varepsilon}$ denotes the virtual interlaminar strain vector. The linearization of (7) is given by the expression

$$\Delta\delta\Pi_{if}(\boldsymbol{u}) = \int_V \delta\boldsymbol{\varepsilon}^T\mathbb{C}\;\Delta\boldsymbol{\varepsilon}\;\mathrm{d}V\,, \qquad \text{with} \qquad \mathbb{C} := \frac{\partial\boldsymbol{\sigma}}{\partial\boldsymbol{\varepsilon}}\,. \tag{8}$$

The virtual and incremental interlaminar strain vectors are defined by

$$\delta\boldsymbol{\varepsilon} = \begin{bmatrix} \delta\gamma_{sn} \\ \delta\gamma_{tn} \\ \delta\varepsilon_n \end{bmatrix} = \begin{bmatrix} \delta u_{s,n} + \delta u_{n,s} \\ \delta u_{t,n} + \delta u_{n,t} \\ \delta u_{n,n} \end{bmatrix}, \quad \Delta\boldsymbol{\varepsilon} = \begin{bmatrix} \Delta\gamma_{sn} \\ \Delta\gamma_{tn} \\ \Delta\varepsilon_n \end{bmatrix} = \begin{bmatrix} \Delta u_{s,n} + \Delta u_{n,s} \\ \Delta u_{t,n} + \Delta u_{n,t} \\ \Delta u_{n,n} \end{bmatrix}, \tag{9}$$

where $\delta\boldsymbol{u} = [\delta u_s, \delta u_t, \delta u_n]^T$ and $\Delta\boldsymbol{u} = [\Delta u_s, \Delta u_t, \Delta u_n]^T$ are the virtual and incremental displacement vectors. The interface is discretized by n_{elem} interface elements. For each we introduce an isoparametric approach with standard trilinear shape functions N_I in natural coordinates $\xi^i = (\xi, \eta, \zeta)$ with $-1 \leq \xi^i \leq 1$ and $\xi^i_I \in \{-1, 1\}$ are employed for node I. Thus, position and displacement vectors can be approximated by

$$\begin{aligned} \boldsymbol{X} &= \sum_{I=1}^{8} N_I\, \boldsymbol{X}_I\,, \quad \text{with} \quad \boldsymbol{X}_I = [X_{Is}, X_{It}, X_{In}]^T\,, \\ \boldsymbol{u} &= \sum_{I=1}^{8} N_I\, \boldsymbol{u}_I\,, \quad \text{with} \quad \boldsymbol{u}_I = [u_{Is}, u_{It}, u_{In}]^T\,, \end{aligned} \tag{10}$$

and

$$\delta\boldsymbol{u} = \sum_{I=1}^{8} N_I\, \delta\boldsymbol{u}_I\,, \quad \Delta\boldsymbol{u} = \sum_{I=1}^{8} N_I\, \Delta\boldsymbol{u}_I\,. \tag{11}$$

Introducing

$$\boldsymbol{B}_I := \begin{bmatrix} N_{I,n} & 0 & N_{I,s} \\ 0 & N_{I,n} & N_{I,t} \\ 0 & 0 & N_{I,n} \end{bmatrix} \tag{12}$$

real, virtual and incremental strain vectors are defined by

$$\boldsymbol{\varepsilon} = \sum_{I=1}^{8} \boldsymbol{B}_I\, \boldsymbol{u}_I\,, \qquad \delta\boldsymbol{\varepsilon} = \sum_{I=1}^{8} \boldsymbol{B}_I\, \delta\boldsymbol{u}_I\,, \qquad \Delta\boldsymbol{\varepsilon} = \sum_{I=1}^{8} \boldsymbol{B}_I\, \Delta\boldsymbol{u}_I\,. \tag{13}$$

With all this in hands we obtain

$$\begin{aligned} \delta\Pi^e_{if} &= \sum_{I=1}^{8} \delta\boldsymbol{u}_I^T \int_V \boldsymbol{B}_I^T \boldsymbol{\sigma}\, \mathrm{d}V &&= \sum_{I=1}^{8} \delta\boldsymbol{u}_I^T \boldsymbol{R}^e_I\,, \\ \Delta\delta\Pi^e_{if} &= \sum_{I=1}^{8}\sum_{K=1}^{8} \delta\boldsymbol{u}_I^T \int_V \boldsymbol{B}_I^T \mathbb{C} \boldsymbol{B}_K\, \mathrm{d}V \Delta\boldsymbol{u}_K &&= \sum_{I=1}^{8}\sum_{K=1}^{8} \delta\boldsymbol{u}_I^T \boldsymbol{K}^e_{TIK} \Delta\boldsymbol{u}_K\,, \end{aligned} \tag{14}$$

where $\boldsymbol{R}^e$ and $\boldsymbol{K}^e_T$ are the element residual vector and the element tangent stiffness matrix. For the integration of the volume integrals in (7) and (8) a Gauss integration scheme may lead to spurious oscillations in the stress field [24]. A Newton-Cotes integration scheme can improve the performance of interface elements [25, 26, 27, 28, 29]. Alfano & Crisfield [30] examined the performance of linear cohesive elements when such an integration is employed. They found that an increase of integration points from 2 to 20 leads to an increase of spurious oscillations. However, for an exact integration of a linear function 3 Newton-Cotes integration points are sufficient. Since cohesive elements are highly non-linear due to their softening behavior a 3x3 Newton-Cotes integration is employed in this work.

3 Comparison of 2D- and 3D-interface elements

In section 2, the governing equations of a 3D-interface element have been derived. In the following we discuss the relations to a typical 2D-formulation with zero thickness. Within the isoparametric concept we use the shape functions

$$N_{I3D} = \frac{1}{8}(1+\xi\xi_I)(1+\eta\eta_I)(1+\zeta\zeta_I) = \frac{1}{2}\, N_{I2D}\, (1+\zeta\zeta_I) \tag{15}$$

and the derivative

$$N_{I3D,\zeta} = N_{I2D}\, \frac{1}{2}\, \zeta_I \,. \tag{16}$$

To calculate cartesian derivatives the introduction of the Jacobian is necessary. It holds in general

$$\boldsymbol{J}_{3D} = \begin{bmatrix} X_{s,\xi} & X_{t,\xi} & X_{n,\xi} \\ X_{s,\eta} & X_{t,\eta} & X_{n,\eta} \\ X_{s,\zeta} & X_{t,\zeta} & X_{n,\zeta} \end{bmatrix} . \tag{17}$$

Here, the special case of no thickness change with $X_{s,\zeta} = X_{t,\zeta} = 0 \;\; X_{n,\xi} = X_{n,\eta} = 0$ and an element thickness h_0 with $X_{n,\zeta} = \dfrac{h_0}{2}$ leads to

$$\boldsymbol{J}_{3D} = \begin{bmatrix} \boldsymbol{J}_{2D} & \boldsymbol{0} \\ \boldsymbol{0} & \dfrac{h_0}{2} \end{bmatrix} \quad \rightarrow \quad \boldsymbol{J}_{3D}^{-1} = \begin{bmatrix} \boldsymbol{J}_{2D}^{-1} & \boldsymbol{0} \\ \boldsymbol{0} & \dfrac{2}{h_0} \end{bmatrix} . \tag{18}$$

Thus, it holds for the cartesian derivative

$$N_{I3D,n} = N_{I3D,\zeta} \cdot \frac{2}{h_0} = \frac{1}{h_0}\, \zeta_I N_{I2D} \,. \tag{19}$$

Within a 2D-interface formulation a material law is introduced between 'stresses' and relative displacements acting as associated 'strains' which are defined as

$$\boldsymbol{\varepsilon}_{2D} = \begin{bmatrix} \gamma_{sn} \\ \gamma_{tn} \\ \varepsilon_n \end{bmatrix} = \begin{bmatrix} \bar{u}_s \\ \bar{u}_t \\ \bar{u}_n \end{bmatrix} = \sum_{I=1}^{8} \underbrace{\zeta_I N_{I2D}}_{\boldsymbol{B}_{2DI}} \boldsymbol{u}_I \,, \tag{20}$$

with $\zeta_i \in \{-1,-1,-1,-1,1,1,1,1\}$. Thus, we have to assume within the strain vector of the 3D-model, Eq. (6), $u_{n,s} = u_{n,t} = 0$ which leads to

$$\boldsymbol{\varepsilon}_{3D} = \sum_{I=1}^{8} \begin{bmatrix} N_{I3D,n} & 0 & 0 \\ 0 & N_{I3D,n} & 0 \\ 0 & 0 & N_{I3D,n} \end{bmatrix} \boldsymbol{u}_I = \sum_{I=1}^{8} N_{I3D,n}\, \boldsymbol{u}_I \,. \tag{21}$$

Taking into account Eq. (19) it holds

$$\boldsymbol{\varepsilon}_{3D} = \sum_{I=1}^{8} \underbrace{\frac{1}{h_0}\, \zeta_I N_{I2D}}_{\boldsymbol{B}_{3DI}} \boldsymbol{u}_I = \sum_{I=1}^{8} \frac{1}{h_0} \boldsymbol{B}_{2DI} = \frac{1}{h_0} \boldsymbol{\varepsilon}_{2D} \,, \tag{22}$$

and similar vectors for virtual and incremental strains. Based on these results one has to derive residual and tangent stiffness matrix, see Eq. (14), for the FE-formulations. At first the volume integration in the 3D-case has to be considered

$$\int_V \mathrm{d}V = \int_n \int_A \mathrm{d}A\, \mathrm{d}n \;=\; h_0 \int_A \mathrm{d}A = h_0 \int_\xi \int_\eta \det \boldsymbol{J}_{2D}\, \mathrm{d}\xi\, \mathrm{d}\eta\,. \tag{23}$$

With the definitions in Eq. (14), the strain relation in Eq.(22) and the integration in Eq. (23) at hand, the following relations between the 2D and 3D-interface formulation can be found

$$\begin{aligned} \boldsymbol{R}^e_{I3D} &= \int_V \boldsymbol{B}^T_{I3D}\boldsymbol{\sigma}_{3D}\,\mathrm{d}V &&= h_0 \int_A \frac{1}{h_0}\boldsymbol{B}^T_{I2D}\mathbb{C}\frac{1}{h_0}\boldsymbol{\varepsilon}_{2D}\,\mathrm{d}A \\ &= \frac{1}{h_0}\int_A \boldsymbol{B}^T_{I2D}\mathbb{C}\boldsymbol{\varepsilon}_{2D}\,\mathrm{d}A &&= \frac{1}{h_0}\boldsymbol{R}^e_{I2D}\,. \end{aligned} \tag{24}$$

$$\begin{aligned} \boldsymbol{K}_{T\,IK3D} &= \int_V \boldsymbol{B}^T_{I3D}\mathbb{C}\boldsymbol{B}_{K3D}\,\mathrm{d}V &&= h_0 \int_A \frac{1}{h_0}\boldsymbol{B}^T_{I2D}\mathbb{C}\frac{1}{h_0}\boldsymbol{B}_{K2D}\,\mathrm{d}A \\ &= \frac{1}{h_0}\int_A \boldsymbol{B}^T_{I2D}\mathbb{C}\boldsymbol{B}_{K2D}\,\mathrm{d}A &&= \frac{1}{h_0}\boldsymbol{K}_{T\,IK2D}\,. \end{aligned} \tag{25}$$

Thus nearly no differences occur. The thickness value h_0 can be used in the 3D-formulation within the material law, see the definition of the *effective* fracture toughness in the next section, see Eq. (42).

4 Cohesive Law

In section 2, the governing equations of a *solid-like* interface element have been established. To simulate delamination, a suitable constitutive law has to be implemented. The cohesive law proposed here is mainly inspired by works of de-Andrés et al. [16] and Ortiz & Pandolfi [17]. They applied their model to the simulation of fracture in metals. Han et al. [31] also applied the model to delamination analysis in honeycomb panels. The softening behavior is dominated by exponential softening and is history-dependent leading to irreversible damage evolution. The absence of any kink in the stress-strain relationships is an advantage worth mentioning. For the formulation of the cohesive law an *effective strain* ε_m which is defined by

$$\varepsilon_m = \sqrt{\beta^2\left(\gamma_{sn}^2 + \gamma_{tn}^2\right) + \langle\varepsilon_n\rangle^2} = \sqrt{\boldsymbol{\varepsilon}^T\boldsymbol{C}\,\boldsymbol{\varepsilon}} \quad \text{with} \quad \boldsymbol{C} := \begin{bmatrix} \beta^2 & 0 & 0 \\ 0 & \beta^2 & 0 \\ 0 & 0 & \frac{\langle\varepsilon_n\rangle}{\varepsilon_n} \end{bmatrix} \tag{26}$$

is introduced. Here, $\langle\bullet\rangle = \frac{1}{2}(\bullet + |\bullet|)$ are the Macauley brackets. The parameter β is a weighting factor which applies different influences for shear mode or mode I delamination. In the following, we employ the convention $\frac{\langle\bullet\rangle}{\bullet} = 0$ if $\bullet = 0$. In the original version of the cohesive law [16, 17, 31] the Macauley brackets are not used in the definition of the effective strain and the bottom right entry of the matrix $\boldsymbol{C}$ is equal to 1. Consequently, compressive normal stresses trigger damage initiation which is assumed to have no physical

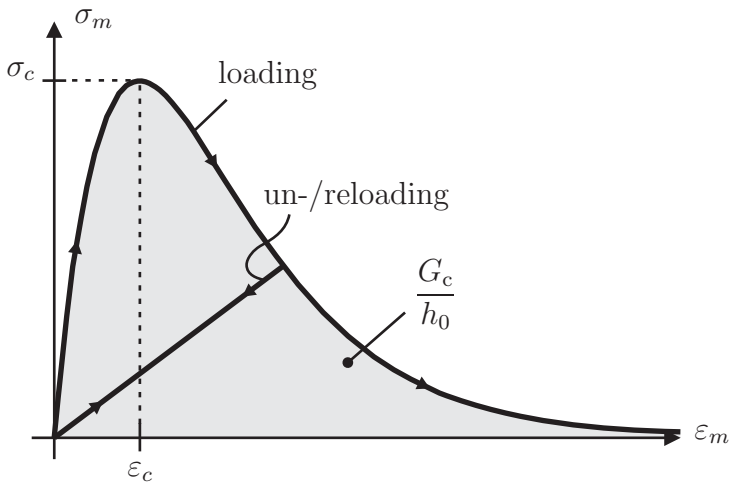

Figure 2: Cohesive law for mixed mode delamination with exponential behavior.

evidence for the case of delamination. Compressive normal stresses might rather complicate the initiation of damage in this case due to inner friction, cf. e.g. PUCK [32]. We postulate the existence of a cohesive free energy function which describes the delamination process. Fig. 2 presents a typical effective stress-effective strain relationship of Smith-Ferrante type [18]. The point of delamination onset is characterized by the limit effective stress σ_c and the corresponding effective strain ε_c. Total decohesion is obtained when the fracture toughness G_c is dissipated completely and the effective stress reverts to zero. For the description of the inelastic softening behavior and in order to avoid the restoration of cohesion within the interface we introduce an internal variable

$$\alpha_k := \max\{\varepsilon_m, \alpha_{k-1}\}\,, \tag{27}$$

where the subscript k denotes the current load step. The subscript k will be omitted in the following when there is no danger of misunderstanding. The internal variable is the maximum effective strain ever observed in the loading history. In order to distinguish loading from unloading a loading function

$$\mathcal{F}(\varepsilon_m - \alpha_{k-1}) = \frac{\langle \varepsilon_m - \alpha_{k-1} \rangle}{\varepsilon_m - \alpha_{k-1}} \tag{28}$$

is introduced, which is equal to 1 in case of loading and zero otherwise. The free energy function associated with Fig. 2 is given by

$$\psi = \psi_1 + \psi_2 = \left[1 - \left(1 + \frac{\alpha}{\varepsilon_c}\right) \mathrm{e}^{-\alpha/\varepsilon_c}\right] + \frac{1}{2}\, K \langle -\varepsilon_n \rangle^2 \,. \tag{29}$$

In [16, 17, 31], the second term in (29) is not applied. We have added this penalty term with the penalty stiffness K to avoid the interpenetration of the crack faces.

The interfacial stress vector can be now derived from the free energy function

$$\boldsymbol{\sigma} = \frac{\partial \psi}{\partial \boldsymbol{\varepsilon}} = \frac{\partial \psi_1(\varepsilon_m, \alpha)}{\partial \varepsilon_m} \, \frac{\partial \varepsilon_m}{\partial \boldsymbol{\varepsilon}} + \frac{\partial \psi_2}{\partial \boldsymbol{\varepsilon}} \,. \tag{30}$$

With $()' = \partial()/\partial\varepsilon_m$ the effective stress can be defined by

$$\sigma_m = \psi_1' = \mathrm{e}\,\sigma_c\,\frac{\alpha}{\varepsilon_c}\,\mathrm{e}^{-\alpha/\varepsilon_c}\,. \tag{31}$$

Substituting (31) in (30) yields

$$\boldsymbol{\sigma} = \frac{\sigma_m}{\varepsilon_m}\,\boldsymbol{C}\,\boldsymbol{\varepsilon} + \boldsymbol{C}_\mathrm{c}\,\boldsymbol{\varepsilon} = (\frac{\sigma_m}{\varepsilon_m}\,\boldsymbol{C} + \boldsymbol{C}_\mathrm{c})\,\boldsymbol{\varepsilon}\,, \tag{32}$$

where $\boldsymbol{C}_\mathrm{c}$ contains the penalty stiffness defined by

$$\boldsymbol{C}_\mathrm{c} = \begin{bmatrix} 0 & 0 & 0 \\ 0 & 0 & 0 \\ 0 & 0 & K\frac{\langle -\varepsilon_n\rangle}{-\varepsilon_n} \end{bmatrix}. \tag{33}$$

From (26), (32) and (33) it follows that

$$\sigma_m = \sqrt{(\boldsymbol{\sigma} - \boldsymbol{C}_\mathrm{c}\,\boldsymbol{\varepsilon})^T\,\boldsymbol{C}^{-1}\,(\boldsymbol{\sigma} - \boldsymbol{C}_\mathrm{c}\,\boldsymbol{\varepsilon})} = \sqrt{\beta^{-2}\,(\tau_{sn}^2 + \tau_{tn}^2) + \langle\sigma_n\rangle^2}\,. \tag{34}$$

As already mentioned, the peak effective stress σ_c is the effective stress at delamination onset. Hence, a criterion for delamination onset is

$$\frac{\sigma_m}{\sigma_c} = 1\,. \tag{35}$$

We assume that a quadratic failure criterion predicts accurately delamination initiation, e.g. Hashin [20] and Mohammadi et al. [33]. Thus, a second criterion is given by

$$\left(\frac{\tau_{sn}}{\tau_{sn}^0}\right)^2 + \left(\frac{\tau_{tn}}{\tau_{tn}^0}\right)^2 + \left(\frac{\langle\sigma_n\rangle}{\sigma^0}\right)^2 = 1\,, \tag{36}$$

with σ^0, τ_{sn}^0 and τ_{tn}^0 the mode I, II and III interlaminar strengths. Using the quadratic interaction criterion expressed by equation (36) yields predictions which agree much better with real life than e.g. maximum stress criteria, cf. Cui et al. [34]. We assume same strengths for pure mode II and III, $\tau_{sn}^0 = \tau_{tn}^0 = \tau^0$. Using the latter conventions in Eq. 36 and using (34) and $\sigma_c = \sigma^0$ in Eq. 35 a comparison of both Eqs. yields

$$\beta = \frac{\tau_0}{\sigma_0}\,, \tag{37}$$

the definition for the material parameter β, which has now physical meaning and can be determined by material testing. The preceding considerations are valid for load progression, which means $\mathcal{F} = 1$. We follow e.g. Camacho & Ortiz [35] and Camanho & Dávila [36] and assume unloading linearly to the origin and reloading on the same path. Thus, the effective stress for $\mathcal{F} = 0$ is expressed by

$$\sigma_m = \frac{\sigma_m(\alpha)}{\alpha}\,\varepsilon_m\,. \tag{38}$$

According to $(8)_2$ the consistent linearization of the stress vector is defined by the partial derivatives of the interlaminar stresses with respect to the interlaminar strains and writes

$$\mathbb{C} = \frac{\partial \boldsymbol{\sigma}}{\partial \boldsymbol{\varepsilon}} = \mathcal{F} \left[\psi_1'' - \frac{\psi_1'}{\alpha} \right] \alpha^{-2} \left(\boldsymbol{C}\boldsymbol{\varepsilon} \right) \left(\boldsymbol{C}\boldsymbol{\varepsilon} \right)^T + \frac{\psi_1'}{\alpha} \boldsymbol{C} + \boldsymbol{C}_{\mathrm{c}} \, . \tag{39}$$

The next aim is to give a physical definition of the penalty stiffness K applied for contact. Consider pure mode I response so the mode I stress in the origin for compression and tension are

$$\sigma_n = \begin{cases} K \, \varepsilon_n & \leftarrow \quad \varepsilon_n \leq 0 \, , \\ \mathrm{e} \, \varepsilon_n \, \dfrac{\sigma_0}{\varepsilon_c} \, \mathrm{e}^{-\varepsilon_n / \varepsilon_c} & \leftarrow \quad \varepsilon_n > 0 \, . \end{cases} \tag{40}$$

One great benefit of the proposed model is that there are no kinks embedded in the effective stress-strain relationships, which should also hold for the penalty term. Thus, we postulate the same stiffness for tension and compression for $\varepsilon_n \to 0$ which leads to

$$\left. \frac{\partial \sigma_n(\varepsilon_n \leq 0)}{\partial \varepsilon_n} \right|_{\varepsilon_n = 0} = \left. \frac{\partial \sigma_n(\varepsilon_n > 0)}{\partial \varepsilon_n} \right|_{\varepsilon_n = 0} \quad \Rightarrow \quad K = \mathrm{e} \, \frac{\sigma_0}{\varepsilon_c} \, . \tag{41}$$

In order to benefit from fracture mechanics approaches the area below the effective stress-strain curve may determine an *effective* fracture toughness which is given by

$$\bar{G}_{\mathrm{c}} = \frac{G_{\mathrm{c}}}{h_0} \, . \tag{42}$$

which leads to objective results with respect to the initial thickness h_0 of the element. The fracture toughness G_{c} in (42) is the mixed mode fracture toughness. For mixed mode I/II loadings, it can be measured by mixed mode bending tests [37] for different mode mixing ratios.

The following relation

$$\bar{G}_c = \frac{G_c}{h_0} = \lim_{\alpha \to \infty} \left\{ \psi_1(\varepsilon_m, \alpha) \right\} = \frac{\mathrm{e} \, \sigma_0 \, \varepsilon_c}{h_0} \, , \tag{43}$$

holds between the effective fracture energy $\bar{G}_c$ and the effective strain at delamination onset ε_c and the peak effective stress σ_c, see Fig. 2. Thus, the penalty stiffness can be calculated

$$K = \frac{(\mathrm{e} \, \sigma_0)^2}{G_{\mathrm{c}}} \, . \tag{44}$$

In order to observe the damage progress inside the interface, typically a damage parameter

$$d = \frac{\hat{\psi}(\alpha)}{\bar{G}_c} \tag{45}$$

is introduced. It defines the ratio between dissipated energy and effective fracture energy and is in the range from 0 (no damage) to 1 (complete decohesion).

5 Numerical Examples

The numerical examples presented in this section show the applicability and the performance of the proposed model. The interface element and the cohesive law have been implemented in an extended version of the finite element program FEAP [40, 41]. The composite structures are modeled with geometrically non-linear quadrilateral shell elements of Reissner-Mindlin type where shear locking effects are reduced by incorporating an *assumed natural strains* (ANS) approach [42]. All material tests have been performed by Korjakins et al. [44] with graphite/epoxy composite IM7/8552. Plate vibration tests according to Rikards et al. [43] have been carried out with uni-directional specimens in order to determine the elastic properties. The results are listed in Table 1.

Table 1: Intralaminar elastic properties of IM7/8552

E_{11} [N/mm^2]	E_{22} [N/mm^2]	G_{12} [N/mm^2]	G_{23} [N/mm^2]	ν_{12}
144000	7700	5900	5900	0.3

5.1 Double Cantilever Beam Test

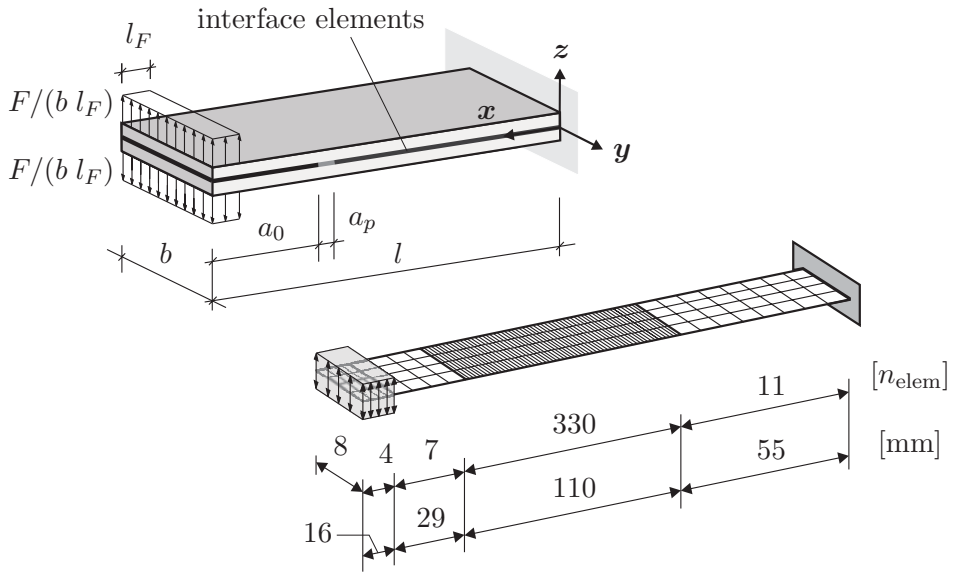

Figure 3: Mechanical device of the DCB test and sketch of the FE discretization.

The numerical example presented first is a double cantilever beam (DCB) test which is a standard testing method for the determination of the mode I fracture toughness [38]. The mechanical device and a sketch of the FE discretization are depicted in Fig. 3. The specimen has a length of $l = 210$ mm and a width of $b = 20$ mm. A pre-crack is generated by insertion of a Teflon layer at the loaded end which has a length of $a_0 = 40$ mm. An additional pre-crack of $a_p = 5$ mm is introduced into the specimen to create a natural crack front. The specimen

is made of 2x12 composite layers of which each has a thickness of $t_l = 0.125$ mm so the overall thickness of the specimen is $2h = 3$ mm. All fibers are oriented in x-direction. The load is introduced through aluminium blocks glued to the specimen at the pre-cracked end. Within the finite element simulation, the aluminium blocks are modeled by distributed loads, Fig. 3. For a rigid body representation of the aluminium blocks, the following boundary conditions and nodal constraints are added: i) In the area of the aluminium blocks the displacement degrees of freedom in y-direction are restrained. ii) In the area of the aluminium blocks the nodal displacements of nodes with same x and z coordinates are linked in z-direction. The specimen is discretized by 8 x (11+330+7+4) finite elements in the x-y plane as depicted in Fig. 3. In thickness direction, the specimen is modeled with 2 eccentric shell elements - each containing 12 composite layers - and 1 interface element except for the pre-cracked area. Here, no interface elements are inserted. The interface elements are located in the middle of the specimen where delamination is expected to propagate. The initial thickness of the interface elements has been chosen to $h_0 = t_l/100$. A similar size has also been used in [14]. The mechanical properties used for the interface elements have been determined by KORJAKINS ET AL. [44] and are listed in Table 2. For pure mode I delamination it holds $G_c = G_{Ic}$.

Table 2: Interlaminar mechanical properties of IM7/8552

σ_0 [N/mm^2]	τ_0 [N/mm^2]	G_{Ic} [N/mm]	G_{IIc} [N/mm]
51.0	115.7	0.270	0.687

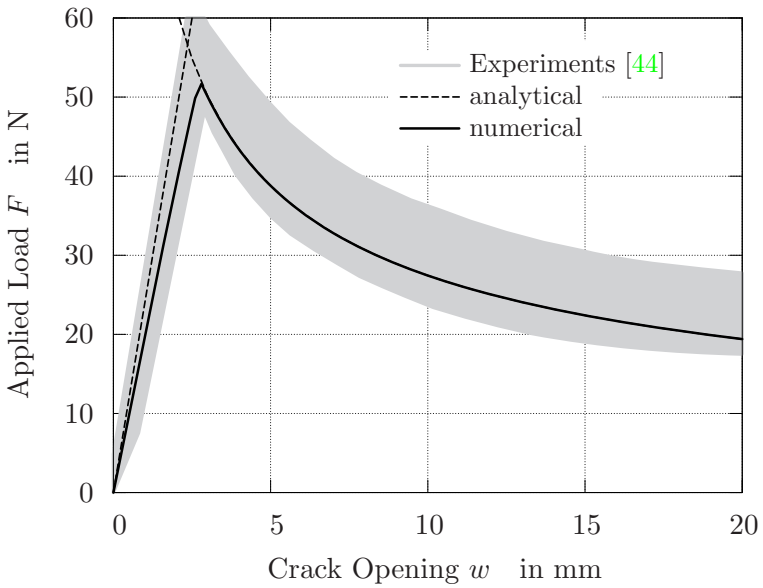

Figure 4: Load-deflection curves of the DCB test

Based on a standard Bernoulli beam theory an approximate analytical solution can be

derived easily. It holds for the undamaged linear part

$$F(w) = \frac{E_{11}\, b\, h^3}{8\, \bar{a}_0^3}\, w \tag{46}$$

and for the part of propagating delamination

$$F(w) = \sqrt{\frac{2b^2}{3w}\sqrt{\frac{G_{Ic}^3 E_{11} h^3}{12}}}\,. \tag{47}$$

Here, F is the resulting load and w the associated crack opening value with $\bar{a}_0 = a_0 + a_p - l_F/2$.

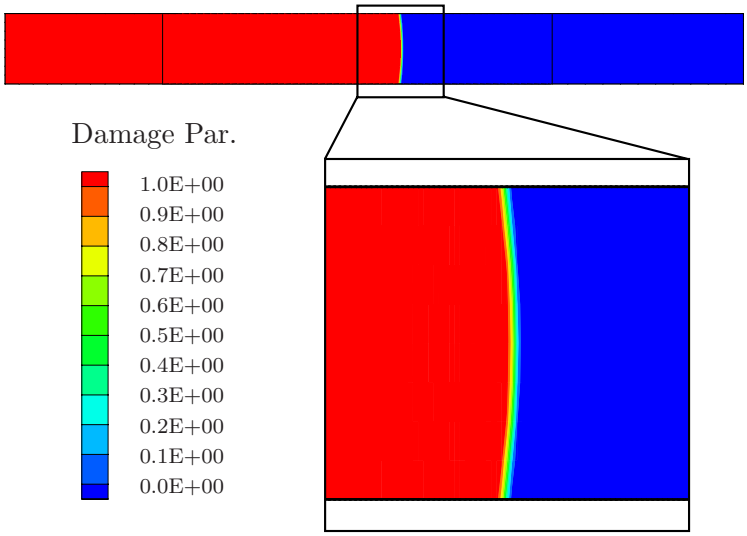

Figure 5: Contour plot of the damage variable at $w = 20$ mm

Fig. 4 shows load-deflection curves of the DCB test. The test results, the analytical and the numerical solution are presented. The finite element approximation is in between the range of test results. In the undamaged linear part the numerical results differs slightly from the analytical stiffness and maximum load. Here, first interface elements begin to fail before the maximum load is reached. In the damage propagation part excellent agreement between the analytical and the numerical solution could be stated.

A contour plot in top view of the damage parameter is presented in Fig. 5 at a crack opening of $w = 20$ mm. The added black lines depict the ends of the fine FE mesh region. In the zoom view a typical slightly curvilinear delamination front can be observed which is caused by transverse bending. This is a usual phenomenon and can also be observed in material tests.

5.2 Rib Stiffened Double Cantilever Beam Test

In the second example we apply the proposed model to skin-stringer separation. A rib stiffened double cantilever beam test is simulated. A T-shaped stiffener is separated from a curved skin. The geometry of the specimen and the loading are depicted in Fig. 6. The curvature radius of the skin is 938 mm in its midplane. The specimen has a length of 250 mm. The skin and the stringer flange have a width of 100 mm and 60 mm, respectively. The

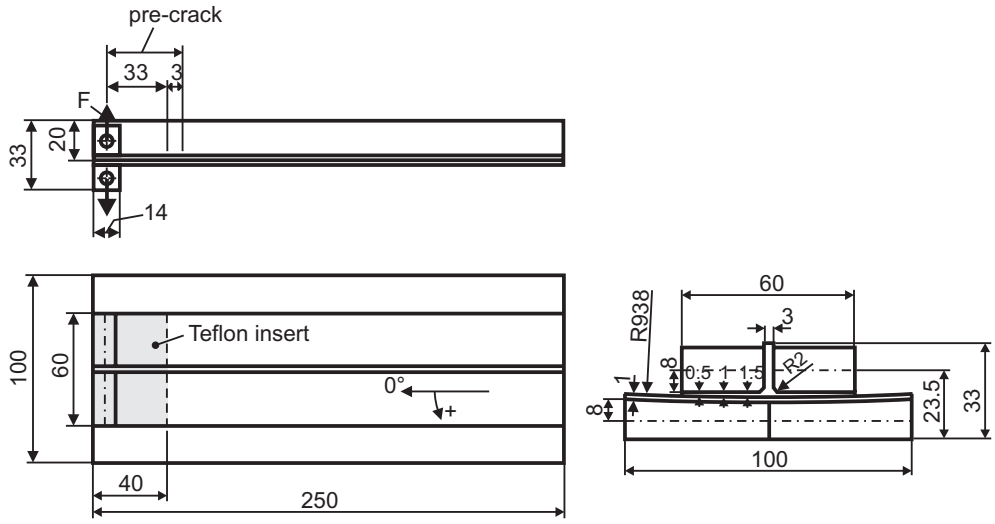

Figure 6: Geometry of the rib-stiffened DCB test

stringer web height is 20 mm. As in the standard DCB test, a Teflon film is inserted at the loaded end between skin and stringer to generate a pre-cracked area. In order to introduce the loading into the specimen, special aluminium blocks are glued to the stringer flanges and the skin at the pre-cracked end. The interface properties used for this example are listed in Table 3. The first value for the fracture energy is the value reported by Korjakins et al. [44]. The second value is a re-calculated arithmetic average. Due to the unsymmetrical stiffness of the specimen, there is no pure mode I but mode I dominated response in the interface elements. The stacking sequences of the skin and the stiffener rib are $[0/45/-45/90]_s$ and

Table 3: Properties for the interface between skin and stiffener made of IM7/8552

σ_0 [N/mm^2]	τ_0 [N/mm^2]	G_c [N/mm]
51.0	115.7	1.103 / 0.875

$[45/-45/0/0]_{3s}$, respectively. Again one layer has a thickness of $t_l = 0.125$ mm and the interface elements have an initial thickness of $h_0 = t_l/100$. The skin and the stiffener flange are discretized by 10 and 6 elements, respectively. The stringer web has 4 elements in radial direction. In the longitudinal direction, $(m_1 + m_2 + m_3 + m_4) = (4 + 240 + 4 + 4)$ elements are used as depicted in Fig. 7. The area of m_4 characterizes the area where the aluminium blocks are located. The area where delamination shall propagate is characterized by m_2 and is 140 mm long. The aluminium blocks are not discretized. In order to obtain an accurate

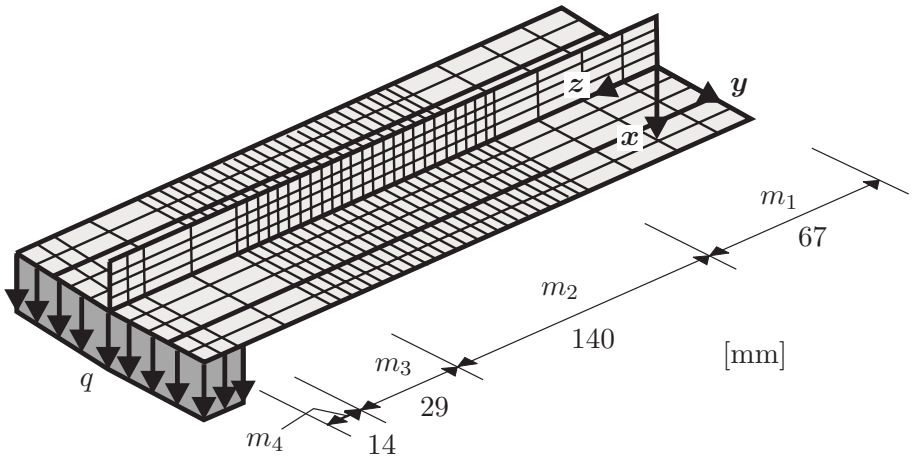

Figure 7: Sketch of finite element mesh

representation of the test the following loading and boundary conditions are applied in the FE-model:

- Displacement degrees of freedom in global z-direction are restrained in the skin and the stringer flange for $z = 243$ mm.
- Displacement degrees of freedom in global x-direction are restrained in the stringer flange for $z = 243$ mm.
- The displacement degrees of freedom in global y-direction where the aluminium block is located are restrained.
- The external load is introduced as distributed load q only into the skin.
- Nodes in the skin and the stringer flange with same coordinates in radial and longitudinal direction are linked in global x-direction where the aluminium blocks are located.

Numerical and material test results are presented in Fig. 8 in terms of load-deflection curves where the applied load F is the resultant from the distributed load q. The associated crack opening w is the displacement of the skin in the global x-direction at $y = 0$, $z = 243$ mm. In general, the simulations agree very well with the test results. The elastic path before delamination onset is slightly overestimated which may be caused by geometrical or material imperfections inside of the test specimens. The degradation paths of delamination propagation are in good agreement with the test results. The choice of the different fracture toughnesses has a slight influence on the maximum load and the stiffness in the degradation path. A quantitatively better prediction could be obtained with the re-calculated value. Fig. 9 shows deformed configurations at different stages of loading for $G_c = 0.875$ N/mm. The increasing crack opening and the propagation of skin-stringer separation can be observed.

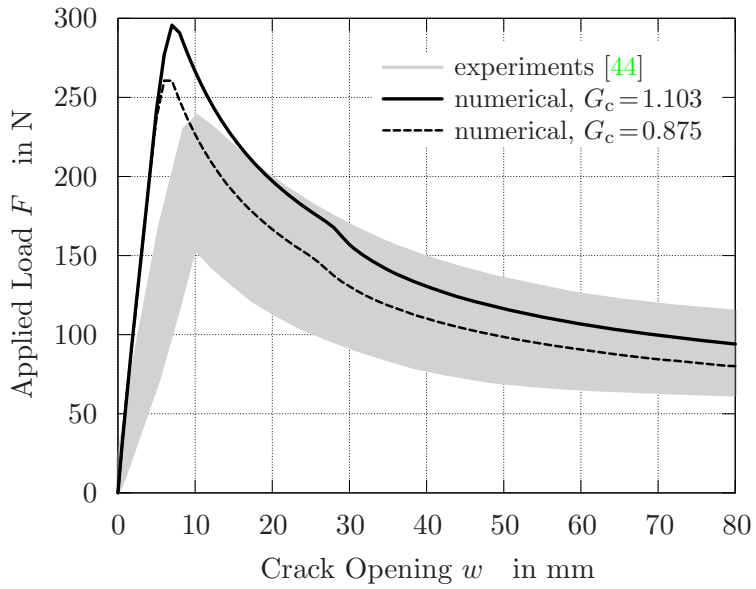

Figure 8: Load-deflection curves of numerical and material test results

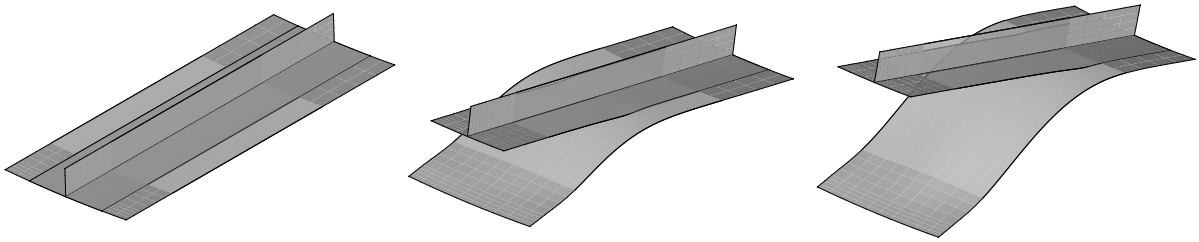

$w = 0.0$ mm $w = 45.0$ mm $w = 90.0$ mm

Figure 9: Deformed configurations at different load stages with $G_c = 0.875$ N/mm

6 Conclusions

A finite element formulation for a solid-like interface element has been derived based on the formulation of standard eight node continuum elements. The constitutive equations have been introduced in the framework of a cohesive zone approach for the interlaminar stresses. Based on publications of DE-ANDRÉS ET AL. [16] and ORTIZ & PANDOLFI [17] the model has been re-formulated in order to exclude damage initiation due to normal compression within the interface. The model contains a quadratic interaction criterion for the prediction of delamination onset under mixed mode loading conditions. The damage progress is expressed in terms of exponential softening. A penalty term is added to avoid the interpenetration of the crack faces. Numerical examples have been presented which showed the applicability of the model to predict skin-stringer separation in laminated composites.

Acknowledgement

This work is supported by the European Commission, Priority Aeronautics and Space, Contract AST3-CT-2003-502723. The information in this paper is provided as is and no guarantee or warranty is given that the information is fit for any particular purpose. The user thereof uses the information at its sole risk and liability.

References

[1] Camanho P.P., Matthews F.L. Delamination onset prediction in mechanically fastened joints in composite laminates. Journal of Composite Materials 1999; 33:906–927. 1

[2] Rybicki E.F., Kanninen M.F. A finite element calculation of stress intensity factors by a modified crack closure integral. Engineering Fracture Mechanics 1977; 9:931–938. 1

[3] Wang G.S., Raju I.S. Strain energy release rate formulae for skin-stringer debond modeled with plate elements. Engineering Fracture Mechanics 1996; 54:211–228. 1

[4] Dugdale D.S. Yielding of steel sheets containing slits. Journal of Mechanics and Physics of Solids 1960; 8:100–104. 1

[5] Barenblatt G.I. Mathematical theory of equilibrium cracks in brittle failure. Advances in Applied Mechanics 1962; 7. 1

[6] Crisfield M., Mi Y., Davies G.A.O., Hellweg H.B. Finite element methods and the progressive failure-modelling of composites structures. In: Owen D.R.J., Oñate E., Hinton E., editors. Computational Plasticity, 239–254. Barcelona: CIMNE, 1997. 1

[7] Needleman A. An analysis of decohesion along an imperfect interface. Int. J. Fract. 1990; 42:21–40. 1

[8] Needleman A. An analysis of tensile decohesion along an interface. J. Mech. Phys. Solids 1990; 38:289–324. 1

[9] Borg R., Nilsson L., Simonsson K. Modeling of delamination using a descretized cohesive zone and damage formulation. Composites Science and Technology 2002; 62:1299–1314. 1

[10] de Borst R., Schipperen J.H.A. Computational methods for delamination and fracture in composites. In: Allix O., Hild F., editors. Continuum Damage Mechanics of Materials and Structures, 325–352. Oxford: Elsevier Science Ltd., 2002. 1

[11] Shet C., Chandra N. Analysis of energy balance when using cohesive zone models to simulate fracture processes. ASME Journal of Engineering Materials and Technology 2002; 124:440–450. 1

[12] Zou Z., Reid S.R., Li S., Soden P.D. Modelling interlaminar and intralaminar damage in filament wound pipes under quasi-static indentation. J. Comp. Mater. 2002; 36:477–499. 1

[13] Zou Z., Reid S.R., Li S. A continuum damage model for delaminations in laminated composites. Journal of the Mechanics and Physics of Solids 2003; 51:333–356. 1

[14] Wagner W., Gruttmann F., Sprenger W. A finite element formulation for the simulation of propagating delaminations in layered composite structures. Int. F. Num. Meth. Engng. 2001; 51:1337–1359. 1, 2, 5.1

[15] Needleman A. A continuum model for void nucleation by inclusion debonding. ASME J. Appl. Mech. 1987; 54:525–531. 1

[16] de-Andrés A., Pérez J.L., Ortiz M. Elastoplastic finite element analysis of three-dimensional fatigue crack growth in aluminium shafts subjected to axial loading. International Journal of Solids and Structures 1999; 36:2231–2258. 1, 4, 4, 4, 6

[17] Ortiz M., Pandolfi A. Finite-deformation irreversible cohesive elements for three-dimensional crack-propagation analysis. Int. J. Numer. Meth. Engng. 1999; 44:1267–1282. 1, 4, 4, 4, 6

[18] Rose J.H., Ferrante J., Smith J.R. Universal binding energy curves for metals and bimetallic interfaces. Phys. Rev. Lett. 1981; 47(9):675–678. 1, 4

[19] Mohr O. Welche Umstände bedingen die Elastizitätsgrenze und den Bruch eines Materials? J. of VDI 24 1900; 45:1524–1530 and 46:1572–1577. 2

[20] Hashin Z. Failure criteria for unidirectional fiber composites. J. Appl. Mech. 1980; 47:329–334. 2, 4

[21] Tvergaard V., Hutchinson J.W. The relation between crack growth resistance and fracture process parameters in elastic-plastic solids. J. Mech. Phys. Solids 1992; 40:1377–1397. 2

[22] Xu X.P., Needleman A. Void nucleation by inclusion debonding in a crystal matrix. Modell. Simul. Mater. Sci. Eng. 1993; 1:111–132. 2

[23] Taylor R.L. Finite element analysis of linear shell problems. In: Whiteman J.R., editor. The Mathematics of Finite Elements and Applications VI (MAFELAP 1987), 191–204. London: Academic Press, 1988. 2

[24] de Borst R., Rots J.G. Occurance of Spurious Mechanisms in Computation of Strain-Softening Solids. Engineering Computations 1989; 6:272–280. 2

[25] Gonçalves J.P., de Moura M.F., de Castro P.T., Marques A.T. Interface Element Including Point-to-Surface Constraints for Three-Dimensional Problems With Damage Propagation. Engineering Computations 2000; 17(1):28–47. 2

[26] Mi Y., Crisfield M.A., Davies G.A.O., Hellweg H.B. Progressive Delamination Using Interface Elements. Journal of Composite Materials 1998; 32:1246–1273. 2

[27] Schellekens J.C.J., de Borst R. Numerical Simulation of Free Edge Delamination in Graphite-Epoxy Laminates Under Uniaxial Tension. In: Proceedings of the 6th International Conference on Composite Structures 1991; 647–657. 2

[28] Schellekens J.C.J. Computational Strategies for Composite Structures, Ph.D. Thesis, Technical University of Delft, 1992. 2

[29] Schellekens J.C.J., de Borst R. On the Numerical Integration of Interface Elements. International Journal for Numerical Methods in Engineering 1993; 36:43–66. 2

[30] Alfano G., Crisfield M.A. Finite Element Interface Elements for the Delamination Analysis of Laminated Composite Structures: Mechanical and Computational Issues. Journal for Numerical Methods in Engineering 2001; 50:1701–1736. 2

[31] Han T.-S., Ural A., Chen C.-S., Zehnder A.T., Ingraffea A.R., Billington S.L. Delamination buckling and propagation analysis of honeycomb panels using a cohesive element approach. Int. Journal of Fracture 2002; 115:101–123. 4, 4, 4

[32] Puck A. Festigkeitsanalyse von Faser-Matrix-Laminaten – Modelle für die Praxis. München/Wien: Carl Hanser Verlag, 1996. 4

[33] Mohammadi S., Owen D.R.J., Peric D. A combined finite/discrete element algorithm for delamination analysis of composites. Finite Elements in Analysis and Design 1998; 28(4):321–336. 4

[34] Cui W., Wisnom M.R., Jones M. A comparison of failure criteria to predict delamination of unidirectional glass/epoxy specimens waisted through the thickness. Composites 1992; 23(3):158–166. 4

[35] Camacho G.T., Ortiz M. Computational modeling of impact damage in brittle materials. Int. J. Solids Struct. 1996; 33:2899–2938. 4

[36] Camanho P.P., Dávila C.G. Mixed-mode decohesion finite elements for the simulation of delamination in composite materials. Technical Report 2002-211737, NASA, 2002. 4

[37] ASTM. Standard test method for mixed mode I-mode II interlaminar fracture toughness of unidirectional fiber reinforced polymer matrix composites. Test Method D6671-01. American Society for Testing and Materials, West Conshohocken, PA, U.S.A., 2002. 4

[38] ASTM. Standard test method for mode I interlaminar fracture toughness of unidirectional fiber-reinforced polymer matrix composites. Test Method D5528-01. American Society for Testing and Materials, West Conshohocken, PA, U.S.A., 2002. 5.1

[39] Testing Methods for Interlaminar Fracture Toughness of Carbon Fiber Reinforced Plastics. Test Method JIS 7086. Japan Industrial Standards, Japanese Standards Association, Tokyo, Japan, 1993.

[40] Taylor R.L. FEAP – A finite element analysis program, version 7.5, theory manual. Department of Civil and Environmental Engineering, University of California at Berkeley, http://www.ce.berkeley.edu/ rlt/feap/theory.pdf, 2003. 5

[41] Taylor R.L. FEAP – A finite element analysis program, version 7.5, user manual. Department of Civil and Environmental Engineering, University of California at Berkeley, http://www.ce.berkeley.edu/ rlt/feap/manual.pdf, 2005. 5

[42] Dvorkin E., Bathe K.J. A continuum mechanics based four node shell element for general nonlinear analysis. Engineering Computations 1984; 1:77–88. 5

[43] Rikards R., Chate A., Steinchen W., Kessler A., Bledzki A.K. Method for identification of elastic properties of laminates based on experiment design. Composites: Part B 1999; 30:279–289. 5

[44] Korjakins A., Ozolinsh O., Rikards R. COCOMAT Technical Report, WP 2, Task 2.2: Investigation of degradation by tests and development of degradation models. Final report, Riga Technical University, Institute of Materials and Structures, Latvia, 2005. 5, 5.1, 5.1, 5.2, 5.2